AARHUS UNIVERSITY

Design of Composite Structures

Reverse Engineering and Structural Analysis of an Unknown Sandwich Beam Under Three-Point Bending

Group 5

Mohammad Khalikujjaman

Ridho Iqbal Maulana

Avi Joshef Gomes

Md Khayrul Islam

Md Abidur Rahman

Submission date: 15 May 2026

Abstract

An unknown lightweight sandwich composite beam was investigated using reverse-engineering methods based on microscopy, dimensional measurements, three-point bending experiments, analytical sandwich beam theory, and COMSOL numerical modelling. The specimens consisted of woven carbon-fibre/epoxy face sheets bonded to an aluminium honeycomb core. Two beam lengths were tested: a long specimen with a 200.000 mm support span and a short specimen with a 100.000 mm support span. From the linear elastic regions of the experimental force–displacement curves, comparison points of 320.778 N at 3.995 mm and 218.521 N at 0.551 mm were selected for the long and short specimens, respectively. An inverse sandwich-beam calculation was used to estimate the dominant face-sheet modulus and core shear modulus, giving $E_f = 66.390$ GPa and $G_c = 146.000$ MPa. These effective properties were implemented in two COMSOL models: a 3D solid model using transversely isotropic stiffness matrices and a shell model using ABD section stiffness matrices. For the long specimen, the 3D solid and shell models predicted 317.300 N and 320.520 N, respectively. For the short specimen, the corresponding predictions were 229.030 N and 206.630 N. The long-beam agreement was excellent, while the short-beam response showed larger deviations due to local support, load-introduction, transverse-shear and core-damage effects. Microscopy and post-failure observations indicate that delamination and core shear failure were the dominant failure mechanisms.

1. Introduction

Sandwich composites are structural materials designed to achieve high bending stiffness at low mass. A typical sandwich panel consists of two thin and stiff face sheets bonded to a lightweight core. The face sheets mainly carry tensile and compressive normal stresses caused by bending, whereas the core keeps the face sheets separated and carries transverse shear stresses. This structural principle gives a high second moment of area without a large mass penalty, making sandwich structures attractive for lightweight mechanical, aerospace, marine and transport applications.

The present work investigates an unknown sandwich beam provided as part of a reverse-engineering exercise. The task was to identify the hidden material and structural properties using experimental evidence, theory and numerical modelling. The available evidence consisted of physical measurements, microscopy images, three-point bending force–displacement data and post-failure observations.

The objective of the project was therefore to estimate the effective layer properties of the unknown sandwich beam and evaluate whether analytical, 3D solid and shell models can reproduce its measured bending response. A further objective was to interpret the likely failure mechanisms by combining force–displacement behaviour, analytical failure criteria, microscopy observations and COMSOL stress distributions.

The work follows an IMRAD structure. The Methods section describes the specimen characterization, three-point bending tests, analytical inverse identification, failure criteria and COMSOL modelling. The Results section presents the estimated material properties, experimental and numerical force–displacement response, and observed failure modes. The Discussion evaluates the modelling assumptions, boundary-condition effects, model fidelity and likely failure mechanisms.

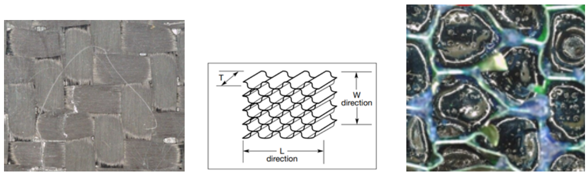

(a) Face sheet **(b)** Core geometry **(c)** Honeycomb core

Figure 1: Material identification of the unknown sandwich beam: (a) woven 0/90 carbon-fibre/epoxy face sheet, (b) schematic of the aluminium honeycomb core geometry, and (c) close-up image of the aluminium honeycomb core cell structure.

2. Methods

2.1. Specimen characterization

The unknown sandwich beam was first examined visually and microscopically. The face material was identified as a woven carbon-fibre reinforced polymer, with a balanced 0/90 architecture and a 2-by-2 twill-like weave pattern. The core was identified as an aluminium honeycomb structure. The face sheets appeared thin and stiff, while the honeycomb core had a low density and a cellular geometry.

The main measured dimensions used in the analytical and numerical models are listed in Table 1. The long and short specimens had the same cross-section and material layup, but different lengths and support spans.

Table 1: Measured geometry used in the analytical and numerical models.

Parameter	Long	Short	Unit
Total length, L	220	120	mm
Support span	200	100	mm
Width, b	20	20	mm
Face thickness, t_f	0.58	0.58	mm
Core thickness, t_c	6.035	6.035	mm
Total thickness, h	7.195	7.195	mm
Specimen mass, m	11.945	6.842	gm

The distance between the centroids of the two face sheets was approximated as

$$d = t_c + t_f, \tag{1}$$

which gives

$$d = 6.035 + 0.58 = 6.615\,\text{mm}. \tag{2}$$

From microscopy, the honeycomb cell diameter was approximately 3.300 mm–3.500 mm. Using the measured cell-wall scale, the estimated core solid volume fraction was approximately

$$V_{f,c} \approx 0.022. \tag{3}$$

This low value confirms that the honeycomb core should not be represented as dense aluminium. Instead, it was treated as an effective cellular continuum with low in-plane stiffness and dominant transverse shear stiffness.

2.2. Three-point bending experiments

Three-point bending tests were conducted under displacement-controlled loading. Each specimen was simply supported and loaded at mid-span. The test machine recorded crosshead displacement, load and time. The force–displacement response was later used to identify the effective stiffness of the sandwich beam and validate the numerical models. After failure, the damaged specimens were also documented using visual inspection, microscopy and the available 3D scan record. The 3D scan information was used qualitatively to support the failure-mode interpretation rather than as a separate quantitative input to the stiffness calculation.

Only the linear elastic region of the force–displacement response was used for inverse identification and COMSOL comparison. The selected experimental comparison points are given in Table 2.

Table 2: Representative experimental points selected from the linear regions of the force–displacement curves for inverse identification and model validation.

Specimen	P [N]	δ [mm]	P/δ [N/mm]
Long	320.778	3.995	80.30
Short	218.521	0.551	396.59

The two span lengths were important for the inverse analysis. The long specimen was more flexible and provided stronger sensitivity to global bending and shear deformation, while the short specimen was stiffer and more sensitive to local loading and support effects.

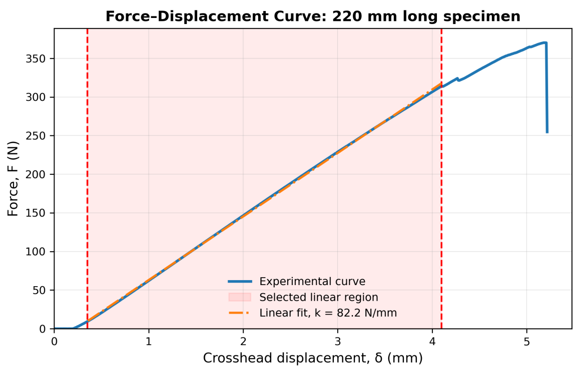

(a) 220 mm long specimen.

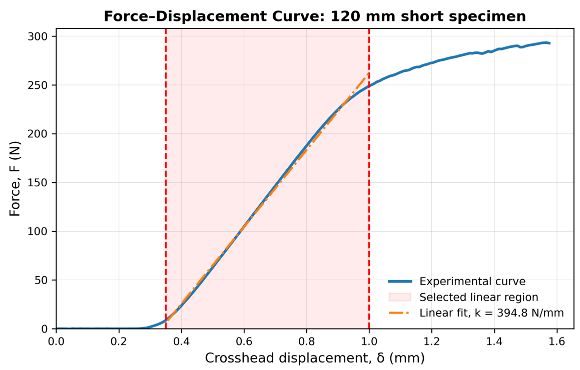

(b) 120 mm short specimen.

Figure 2: Experimental force–displacement curves for the 220 mm and 120 mm specimens. The red dashed lines indicate the selected approximately linear regions, while the orange dashed line represents the linear fit used to estimate experimental stiffness.

The red dashed lines in the force–displacement plots indicate the approximately linear regions used for inverse identification. Within these regions, representative experimental points were selected for model validation, as listed in Table 2. The ratio P/δ was used as the experimental stiffness estimate for each specimen.

2.3. Analytical sandwich-beam model

For a sandwich beam under three-point bending, the total mid-span deflection was assumed to be the sum of bending deflection and transverse shear deflection,

$$\delta = \delta_b + \delta_s. \tag{4}$$

For a simply supported beam loaded by a central point load,

$$\delta_b = \frac{PL^3}{48D}, \tag{5}$$

and

$$\delta_s = \frac{PL}{4S}, \tag{6}$$

where P is the applied load, L is the support span, D is the effective bending stiffness of the sandwich section, and S is the effective transverse shear stiffness. Therefore,

$$\delta = P\left(\frac{L^3}{48D} + \frac{L}{4S}\right). \tag{7}$$

The bending stiffness of a symmetric sandwich beam is dominated by the face sheets because the faces are far from the neutral axis. The equivalent bending stiffness was written as

$$D = E_f\left[2\left(\frac{bt_f^3}{12} + bt_f\left(\frac{d}{2}\right)^2\right)\right], \tag{8}$$

or equivalently,

$$D = E_f\left(\frac{bt_f^3}{6} + \frac{bt_f d^2}{2}\right). \tag{9}$$

The term $bt_f d^2/2$ dominates because the face sheets are separated by the honeycomb core. The local bending term $bt_f^3/6$ is much smaller but was retained for improved accuracy.

The transverse shear stiffness was represented mainly by the honeycomb core,

$$S = G_c bt_c, \tag{10}$$

where G_c is the effective core shear modulus. Substituting Eqs. (9) and (10) into Eq. (7) gives

$$\delta = P\left[\frac{L^3}{48E_f\left(\frac{bt_f^3}{6} + \frac{bt_f d^2}{2}\right)} + \frac{L}{4G_c bt_c}\right]. \tag{11}$$

The long and short experimental points then give two equations with two unknowns, E_f and G_c,

$$\delta_L = P_L\left[\frac{L_L^3}{48E_f\left(\frac{bt_f^3}{6} + \frac{bt_f d^2}{2}\right)} + \frac{L_L}{4G_c bt_c}\right], \tag{12}$$

$$\delta_S = P_S\left[\frac{L_S^3}{48E_f\left(\frac{bt_f^3}{6} + \frac{bt_f d^2}{2}\right)} + \frac{L_S}{4G_c bt_c}\right]. \tag{13}$$

Solving the two equations gave the effective properties

$$E_f = 66.390\,\text{GPa}, \tag{14}$$

and

$$G_c = 146.000\,\text{MPa}. \tag{15}$$

These values are effective structural properties identified from the beam response. They should not be interpreted as pure coupon material constants, because they include the influence of weave architecture, bonding, honeycomb geometry and experimental assumptions.

2.4. Material model selection

The real sandwich beam is anisotropic. The woven face sheets are stiff in the fibre directions, while the honeycomb core is much stiffer through the thickness than in the in-plane directions. A full orthotropic elastic model would require

$$E_1, E_2, E_3, G_{12}, G_{13}, G_{23}, \nu_{12}, \nu_{13}, \nu_{23} \tag{16}$$

for each constituent. These constants cannot be uniquely identified from only two three-point bending tests. A fully orthotropic model would therefore require many uncertain assumptions.

An isotropic model was also considered unsuitable for the honeycomb core. For an isotropic material,

$$G = \frac{E}{2(1+\nu)}. \tag{17}$$

Thus, matching the measured core shear modulus would automatically create an unrealistic in-plane Young's modulus for the honeycomb. In the real core, the cell walls bend and rotate easily in-plane, while the structure remains relatively stiff in transverse shear.

A transversely isotropic model was therefore selected as the best compromise. This allows

$$E_1 = E_2 \neq E_3, \tag{18}$$

and

$$G_{13} = G_{23} \neq G_{12}. \tag{19}$$

For the face sheets, the balanced 0/90 woven architecture was approximated by

$$E_1 \approx E_2 = 66.390\,\text{GPa}. \tag{20}$$

For the honeycomb core, the important property in three-point bending was the transverse shear modulus,

$$G_{13} = G_{23} = 146.000\,\text{MPa}. \tag{21}$$

2.5. Analytical failure criteria

Four possible failure modes were considered: face failure, face wrinkling, core shear failure and debonding.

Face failure was checked by comparing the estimated face stress with a representative face strength,

$$\sigma_f \geq \sigma_{f,\text{crit}}. \tag{22}$$

The maximum bending moment under a central load is

$$M_{\max} = \frac{PL}{4}. \tag{23}$$

The face stress was estimated from the sandwich bending relation,

$$\sigma_f = E_f \frac{M_{\max}(d/2)}{D}. \tag{24}$$

Face wrinkling was checked using

$$\sigma_f \geq \sigma_{wr}, \tag{25}$$

where σ_{wr} is the critical wrinkling stress.

Core shear failure was checked from the average shear stress in the core. The shear force in a three-point bending beam is approximately

$$V = \frac{P}{2}, \tag{26}$$

and the average core shear stress is

$$\tau_c = \frac{V}{bt_c} = \frac{P}{2bt_c}. \tag{27}$$

The failure condition is

$$\tau_c \geq \tau_{c,\text{crit}}. \tag{28}$$

Debonding was treated as an interface failure between the face sheet and core. In simplified stress form, the screening criterion was written as

$$\sigma_{\text{interface}} \geq \sigma_{\text{debond,crit}}. \tag{29}$$

For transparency, the interface value reported in Table 5 was evaluated as a simplified amplified interface-stress indicator,

$$\sigma_{\text{interface}} \approx K_{\text{int}}\sigma_f, \qquad K_{\text{int}} = 4, \tag{30}$$

where K_{int} represents the local amplification associated with load introduction and stress transfer between the face sheet and honeycomb core. This estimate was used only to rank the likelihood of debonding and not as a calibrated fracture-mechanics criterion.

This is a simplified failure screening rather than a full fracture-mechanics analysis. A more rigorous debonding model would require interfacial fracture toughness and energy release rate.

2.6. 3D solid COMSOL model

A 3D solid model was created in COMSOL for both specimens. The geometry was divided into three bonded layers: bottom face sheet, honeycomb core and top face sheet. The long model used a 220.000 mm length and 200.000 mm support span, while the short model used a 120.000 mm length and 100.000 mm support span.

The face and core were assigned transversely isotropic linear elastic material behaviour through a full 6-by-6 stiffness matrix in Voigt notation,

$$\boldsymbol{\sigma} = \mathbf{C}\boldsymbol{\varepsilon}. \tag{31}$$

The MATLAB script first constructed the compliance matrix

$$\mathbf{S} = \begin{bmatrix} 1/E_1 & -\nu_{21}/E_2 & -\nu_{31}/E_3 & 0 & 0 & 0 \\ -\nu_{12}/E_1 & 1/E_2 & -\nu_{32}/E_3 & 0 & 0 & 0 \\ -\nu_{13}/E_1 & -\nu_{23}/E_2 & 1/E_3 & 0 & 0 & 0 \\ 0 & 0 & 0 & 1/G_{23} & 0 & 0 \\ 0 & 0 & 0 & 0 & 1/G_{13} & 0 \\ 0 & 0 & 0 & 0 & 0 & 1/G_{12} \end{bmatrix} \tag{32}$$

using reciprocal Poisson's ratios. The stiffness matrix was then obtained as

$$\mathbf{C} = \mathbf{S}^{-1}. \tag{33}$$

The resulting matrices were entered in COMSOL using the anisotropic linear elastic material option. The three-point bending setup was represented using support and loading regions. A prescribed displacement was applied at the centre loading patch, and the reaction force was extracted using a probe.

2.7. ABD shell COMSOL model

A second numerical model was developed using COMSOL Shell physics. The sandwich beam was represented by its mid-surface, and the laminate section stiffness was entered directly using the Section Stiffness material option. The shell model used the laminate relation

$$\begin{bmatrix} \mathbf{N} \\ \mathbf{M} \end{bmatrix} = \begin{bmatrix} \mathbf{A} & \mathbf{B} \\ \mathbf{B} & \mathbf{D} \end{bmatrix} \begin{bmatrix} \boldsymbol{\varepsilon}_0 \\ \boldsymbol{\kappa} \end{bmatrix}, \tag{34}$$

where $\mathbf{N}$ and $\mathbf{M}$ are the membrane force and moment resultants, $\boldsymbol{\varepsilon}_0$ is the mid-plane strain vector, and $\boldsymbol{\kappa}$ is the curvature vector.

For each layer k, the laminate stiffness matrices are

$$\mathbf{A} = \sum_{k=1}^{n} \bar{\mathbf{Q}}_k (z_k - z_{k-1}), \tag{35}$$

$$\mathbf{B} = \frac{1}{2} \sum_{k=1}^{n} \bar{\mathbf{Q}}_k (z_k^2 - z_{k-1}^2), \tag{36}$$

and

$$\mathbf{D} = \frac{1}{3} \sum_{k=1}^{n} \bar{\mathbf{Q}}_k (z_k^3 - z_{k-1}^3). \tag{37}$$

Because the layup was symmetric,

$$\text{face}/\text{core}/\text{face}, \tag{38}$$

the bending-extension coupling matrix was zero,

$$\mathbf{B} = \mathbf{0}. \tag{39}$$

COMSOL shell theory also required a transverse shear stiffness matrix. The core-dominated shear stiffness was estimated as

$$A_{s,xz} = A_{s,yz} = G_c t_c, \tag{40}$$

which gives

$$A_s = 146 \times 10^6 \times 6.035 \times 10^{-3} = 8.811 \times 10^5 \text{ N/m}. \tag{41}$$

The final matrices entered in COMSOL were

$$\mathbf{A} = \begin{bmatrix} 7.7212\times10^7 & 3.8623\times10^6 & 0 \\ 3.8623\times10^6 & 7.7212\times10^7 & 0 \\ 0 & 0 & 5.8023\times10^6 \end{bmatrix} \text{N/m}, \tag{42}$$

$$\mathbf{B} = \mathbf{0}, \tag{43}$$

$$\mathbf{D} = \begin{bmatrix} 846.78 & 42.344 & 0 \\ 42.344 & 846.78 & 0 \\ 0 & 0 & 63.619 \end{bmatrix} \text{N m}, \tag{44}$$

and

$$\mathbf{A_s} = \begin{bmatrix} 8.811\times10^5 & 0 \\ 0 & 8.811\times10^5 \end{bmatrix} \text{N/m}. \tag{45}$$

The same ABD matrices were used for both the long and short shell models because both specimens had the same layup and cross-section. Only the length, support span, support positions and prescribed displacement were changed.

3. Results

3.1. Inverse material properties

The inverse sandwich-beam calculation identified the effective face modulus and core shear modulus listed in Table 3.

Table 3: Effective material properties identified from the linear bending response.

Property	Value	Main role
E_f	66.390 GPa	Face bending stiffness
G_c	146.000 MPa	Core shear stiffness
t_f	0.580 mm	Face contribution to D
t_c	6.035 mm	Core contribution to S

These values were subsequently used in both the transversely isotropic 3D solid model and the ABD-based shell model.

3.2. Experimental and numerical force–displacement response

The force–displacement curves from COMSOL were linear over the investigated range, as expected from the linear elastic material definition. Table 4 compares the experimental and numerical reaction forces at the selected displacements.

Table 4: Comparison of experimental, 3D solid and shell reaction forces.

Specimen	Model	Displacement [mm]	Reaction force [N]	Stiffness [N/mm]	Error vs. experiment
Long	Experiment	3.995	320.778	80.30	–
Long	3D solid COMSOL	3.995	317.30	79.42	-1.08%
Long	Shell COMSOL	3.995	320.52	80.23	-0.08%
Short	Experiment	0.551	218.521	396.59	–
Short	3D solid COMSOL	0.551	229.03	415.66	+4.81%
Short	Shell COMSOL	0.551	206.63	375.01	-5.44%

For the long specimen, both numerical models reproduced the experimental stiffness very accurately. The 3D solid model gave 317.300 N, corresponding to an error of −1.08%, while the shell model gave 320.520 N, corresponding to an error of only −0.08%.

For the short specimen, the 3D solid model predicted 229.030 N, which is +4.81% above the experiment. The shell model predicted 206.630 N, which is −5.44% below the experiment. These deviations are still reasonable, but they show that the short beam is more sensitive to local loading, support and transverse shear effects.

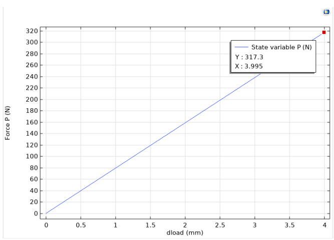

(a) Long specimen: 3D solid model.

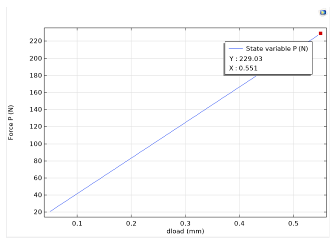

(b) Short specimen: 3D solid model.

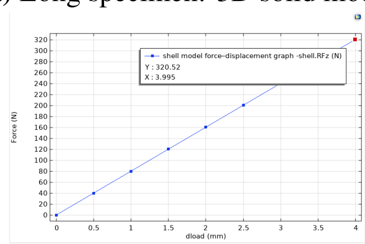

(c) Long specimen: shell model.

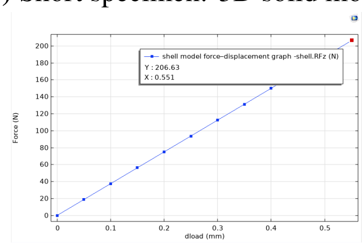

(d) Short specimen: shell model.

Figure 3: COMSOL force–displacement response for the 3D solid and shell models. The long specimen was reproduced very accurately by both approaches, whereas the short specimen showed larger sensitivity to modelling assumptions.

3.3. Stress distributions

The 3D solid stress plots showed the expected bending stress distribution. The largest axial stresses occurred near mid-span, with tension on one face sheet and compression on the opposite face sheet. This confirms that the face sheets carried the main bending load. The core experienced lower axial stress but carried the transverse shear load.

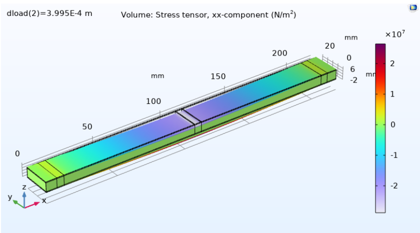

(a) Long specimen: 3D solid model, axial stress σ_{xx}.

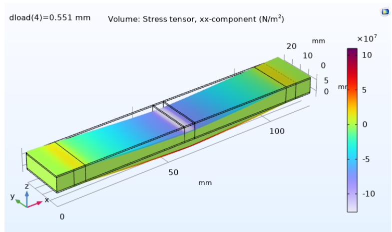

(b) Short specimen: 3D solid model, axial stress σ_{xx}.

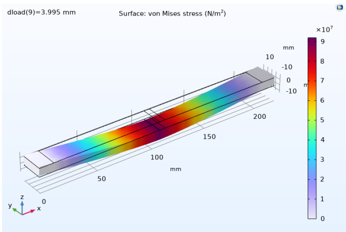

(c) Long specimen: shell model, von Mises stress.

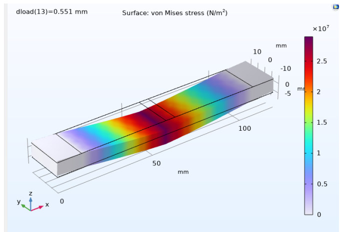

(d) Short specimen: shell model, von Mises stress.

Figure 4: Representative COMSOL stress distributions for the long and short specimens. The 3D solid model resolves layer-level axial stress patterns, while the shell model represents the global section response using ABD stiffness.

The shell model also predicted maximum stresses near the centre loading region. However, the shell model does not explicitly represent the individual face and core layers after the ABD stiffness is assigned. Therefore, shell stresses are most useful for global response comparison, while layer-specific stress interpretation is better supported by the 3D solid model and analytical reconstruction.

3.4. Failure assessment

The analytical failure assessment is summarized in Table 5. The values should be interpreted as a screening calculation because representative critical strengths were used.

Table 5: Analytical failure screening for the long and short specimens.

Failure mode	Long stress	Short stress	Critical value	Interpretation
Face failure	114.690 MPa	38.990 MPa	600.000 MPa	Safe
Face wrinkling	114.690 MPa	38.990 MPa	1097.000 MPa	Safe
Core shear failure	1.300 MPa	0.904 MPa	1.350 MPa	Long critical; short near-critical
Debonding	457.900 MPa	155.990 MPa	339.000 MPa	Long fails; short below critical

Face failure and face wrinkling were not predicted to be critical. The core shear stress was close to the assumed core shear strength, especially for the long specimen. The debonding criterion predicted failure for the long specimen and a safer value for the short specimen.

Post-failure microscopy supported these results. The long specimen showed extensive delamination and core-related damage, while the short specimen showed local core damage and partial delamination. Clear global face wrinkling was not observed.

(a) Face cracking **(b)** Core failure **(c)** Debonding

Figure 5: Post-failure observations of the sandwich beam specimens showing face cracking, core failure and debonding/delamination.

The images indicate that clear global face wrinkling was not observed, while core shear damage and face/core delamination were the dominant failure mechanisms.

4. Discussion

4.1. Validity of the inverse identification

The inverse identification method gave effective properties that reproduced the global force–displacement response with good accuracy. The two-span test strategy was important because bending and shear contributions scale differently with span length. The bending term in Eq. (7) scales with L^3, while the shear term scales with L. Therefore, using both a long and a short specimen made it possible to estimate both E_f and G_c from the experimental data.

The identified modulus $E_f = 66.390\,\text{GPa}$ represents the effective in-plane stiffness of the woven face sheets in the beam direction. The identified $G_c = 146.000\,\text{MPa}$ represents the effective transverse shear stiffness of the honeycomb core. These are not exact constituent material properties; they are homogenized values suitable for reproducing the structural response of the tested sandwich beams.

4.2. 3D solid model versus shell model

The 3D solid model is the more detailed numerical approach because it explicitly represents the top face, core and bottom face as separate volumes. It is therefore more suitable for visualizing through-thickness stress distributions and local stress concentrations near the support and loading regions. This is important for failure interpretation, especially when core shear failure or debonding is expected.

The shell model is computationally simpler and efficient. It represents the sandwich beam using an equivalent section stiffness. The very good agreement for the long beam confirms that the ABD-based model is highly suitable for global stiffness prediction when the section stiffness is known. However, the shell model cannot directly resolve the individual face/core layer stresses because the layer information is condensed into the ABD matrices. Through-thickness stresses from the shell model must therefore be reconstructed analytically if layer-specific values are required.

4.3. Boundary-condition effects

Boundary conditions are a major source of uncertainty in three-point bending simulations. In the experiment, the loading nose and supports contact the specimen over finite regions. This can introduce local indentation, friction, local crushing and non-uniform pressure. In the COMSOL models, the boundary conditions were idealized using prescribed displacement and support regions or shell support lines.

The long beam was less sensitive to these simplifications because its response was dominated by global bending and shear over the full span. The short beam was more sensitive because the smaller span increases the relative importance of local load introduction, support effects and core deformation. This explains why the short-beam model errors were larger than the long-beam errors.

4.4. Failure mechanism interpretation

The analytical failure screening, force–displacement curves and microscopy observations indicate that face yielding and face wrinkling were not the governing failure modes. The estimated face stresses were well below the assumed face strength and wrinkling limits. This agrees with the visual observation that no clear global face wrinkling occurred.

For the long specimen, the force–displacement curve was nearly linear until a sudden load drop. This indicates brittle failure after elastic energy storage. The analytical debonding criterion exceeded the assumed critical value, and microscopy showed extensive delamination. Therefore, the most likely initial failure mechanism for the long beam was debonding, followed by core shear damage and local face cracking.

For the short specimen, the response showed stronger nonlinear behaviour before failure. This suggests progressive local damage. The analytical screening indicated that global debonding was below the assumed critical value, but the core shear stress was still high. Microscopy showed core damage and partial delamination. Therefore, the short-beam failure was likely governed by local core crushing, cell-wall buckling, imperfections or local loading damage, followed by partial delamination.

4.5. Limitations

Several limitations should be noted. First, the face sheet was treated as an equivalent transversely isotropic material, although the real twill weave contains fibre undulation, resin-rich pockets and local thickness variation. Second, the honeycomb was homogenized as a continuum even though the actual core consists of discrete aluminium cell walls. Third, the experimental displacement was based on machine crosshead displacement, which may include compliance and local indentation. Fourth, the critical strengths used in the failure assessment were representative values rather than directly measured material strengths. Finally, the COMSOL models used idealized bonded interfaces and did not include progressive damage, nonlinear contact or delamination growth.

Despite these limitations, the agreement between experiment, analytical identification and numerical simulation is strong. The modelling approach is therefore sufficient for identifying the dominant stiffness parameters and explaining the observed failure mechanisms.

5. Conclusion

An unknown sandwich composite beam was reverse engineered using microscopy, three-point bending tests, analytical sandwich theory and COMSOL simulations. The beam consisted of woven 0/90 carbon-fibre/epoxy face sheets bonded to an aluminium honeycomb core. The measured cross-section had a width of 20.000 mm, face-sheet thickness of 0.580 mm, core thickness of 6.035 mm and total thickness of approximately 7.200 mm.

Analytical inverse identification from the long and short three-point bending responses gave an effective face-sheet modulus of $E_f = 66.390$ GPa and an effective core shear modulus of $G_c = 146.000$ MPa. These values were implemented in a transversely isotropic 3D solid COMSOL model and an ABD-based shell model.

For the long specimen, the experimental reaction force was 320.778 N at 3.995 mm. The 3D solid model predicted 317.300 N, and the shell model predicted 320.520 N. For the short specimen, the experimental reaction force was 218.521 N at 0.551 mm. The 3D solid model predicted 229.030 N, while the shell model predicted 206.630 N. The long-beam agreement was excellent, while the larger short-beam deviations were attributed to local support, load-introduction, transverse-shear and core-damage effects.

The failure analysis indicated that face yielding and face wrinkling were unlikely. The dominant failure mechanisms were core shear failure and delamination. For the long specimen, debonding was likely the initial failure mode, followed by core shear damage. For the short specimen, local core damage and partial delamination were more likely due to local crushing, cell-wall buckling and damage accumulation. Overall, the combination of analytical identification, 3D solid modelling, shell modelling and microscopy provided a consistent explanation of the unknown sandwich beam response.

Author contributions

All group members contributed to the laboratory work, data processing, analytical calculations, COMSOL modelling, result interpretation and report writing.

Appendix A – 3D Solid COMSOL Models

Appendix B – ABD - Based Shell COMSOL Models

Appendix C – MATLAB Scripts

Appendix D – Experimental Data

Appendix E – Processed Data and Plots

Appendix F – AI Declaration Form